

UC Riverside

UC Riverside Previously Published Works

Title

Role of Molecular Interactions and Protein Rearrangement in the Dissociation Kinetics of p38 α MAP Kinase Type-I/II/III Inhibitors

Permalink

<https://escholarship.org/uc/item/71j3w1zj>

Journal

Journal of Chemical Information and Modeling, 58(5)

ISSN

1549-9596

Authors

You, Wanli
Chang, Chia-en A

Publication Date

2018-05-29

DOI

10.1021/acs.jcim.7b00640

Peer reviewed



Published in final edited form as:

J Chem Inf Model. 2018 May 29; 58(5): 968–981. doi:10.1021/acs.jcim.7b00640.

Role of Molecular Interactions and Protein Rearrangement in the Dissociation Kinetics of p38 α MAP Kinase Type-I/II/III Inhibitors

Wanli You and Chia-en A. Chang*

Department of Chemistry, University of California at Riverside, Riverside, California 92521, United States

Abstract

Understanding the governing factors of fast or slow inhibitor binding/unbinding assists in developing drugs with preferred kinetic properties. For inhibitors with the same binding affinity targeting different binding sites of the same protein, the kinetic behavior can profoundly differ. In this study, we investigated unbinding kinetics and mechanisms of fast (type-I) and slow (type-II/III) binders of p38 α mitogen-activated protein kinase, where the crystal structures showed that type-I and type-II/III inhibitors bind to pockets with different conformations of the Asp-Phe-Gly (DFG) motif. The work used methods that combine conventional molecular dynamics (MD), accelerated molecular dynamics (AMD) simulations, and the newly developed pathway search guided by internal motions (PSIM) method to find dissociation pathways. The study focuses on revealing key interactions and molecular rearrangements that hinder ligand dissociation by using umbrella sampling and post-MD processing to examine changes in free energy during ligand unbinding. As anticipated, the initial dissociation steps all require breaking interactions that

*Corresponding Author: chiaenc@ucr.edu. Telephone: (951) 827-7263 (C.A.C.).

Supporting Information

The Supporting Information is available free of charge on the ACS Publications website at DOI: 10.1021/acs.jcim.7b00640. Simulations performed for each system (Table S1); an example of fragmentation of HIV-1 protease (HIVp) for multilayer internal coordinate definition (Figure S1); overview of the algorithm in one search branch used in PSIM (Figure S2); reconstruction of dissociation path from AMD; dissociation path of SB2 from p38 α with a DFG-in conformation is rebuilt from two 10 ns CMD (Figure S3); RMSD of heavy backbone atoms in trajectories of CMD, low boost AMD and high boost AMD relative to crystal structure (Figure S4); free energy principal component projection of (A) 100 ns CMD, (B) 100 ns low boost AMD, and (C) 100 ns high boost AMD onto (PC1, PC2) defined by the 100 ns high boost AMD (Figure S5); snapshots from PSIM trajectory of dissociation process of SB2 (DFG-in) (Figure S6); PMF of dissociation process of SB2 (DFG-out) and the selected snapshots from US (Figure S7); snapshots from PSIM trajectory of dissociation process of SB2 (DFG-out) (Figure S8); PMF of dissociation process of SK8 and selected snapshots from US (Figure S9); snapshots from PSIM trajectory of dissociation process of SK8 (Figure S10); PMF of SB2 (DFG-in) dissociation (blue curve) and profile of number of pocket-water (red curve) as a function of the RC distance (Figure S11); snapshots from PSIM trajectory of dissociation process of BIRB796 (Figure S12); PMF of dissociation process of LIG4 along allosteric pathway and selected snapshots from US (Figure S13); PMF of dissociation process of LIG4 along ATP pathway and selected snapshots from US (Figure S14); PMF of BIRB796 dissociation (blue curve) and profile of number of pocket-water (red curve) as a function of the RC distance (Figure S15); the first PC modes of free DFG-in and DFG-out proteins from CMD simulations (Figure S16); correlation maps of free DFG-in and DFG-out proteins from CMD simulations (Figure S17); RMSF of Ca of p38 α complexes and free proteins from CMD simulations (Figure S18); correlation maps of p38 α complexes from CMD simulations (Figure S19); free energy change along hinge movement of p38 α in DFG-out conformation at different stages of dissociation of LIG4 (Figure S20); free energy change along hinge movement of p38 α at different stages of dissociation of SB2 (DFG-out) and SK8 (Figure S21) (PDF)

Movie of BIRB796 and LIG4 moving further toward the ATP binding site (AVI)

Movie of BIRB796 and LIG4 unbinding directly from the allosteric pocket (AVI)

ORCID

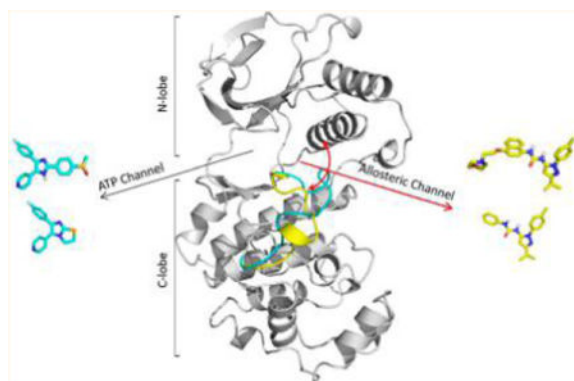
Chia-en A. Chang: 0000-0002-6504-8529

Notes

The authors declare no competing financial interest.

appeared in crystal structures of the bound complexes. Interestingly, for type-I inhibitors such as SB2, p38 α keeps barrier-free conformational fluctuation in the ligand-bound complex and during ligand dissociation. In contrast, with a type-II/III inhibitor such as BIRB796, with the rearrangements of p38 α in its bound state, ligand unbinding features energetically unfavorable protein–ligand concerted movement. Our results also show that the type-II/III inhibitors preferred dissociation pathways through the allosteric channel, which is consistent with an existing publication. The study suggests that the level of required protein rearrangement is one major determining factor of drug binding kinetics in p38 α systems, providing useful information for development of inhibitors.

Graphical abstract



INTRODUCTION

The study of small molecular kinase inhibitors has been the central focus in drug discovery in the past decade.^{1–5} To develop a good inhibitor, the compound must have strong binding affinity to compete with the natural substrate. In addition, drug binding residence time, the mean value for a drug staying in the binding pocket, which can be approximated by a dissociation rate constant, $1/k_{\text{off}}$, may be crucial in drug efficacy and increase drug selectivity.^{6–14} However, although fine-tuning drug binding kinetics is highly desired, we need further understanding of the contribution of a drug's chemical structure and ligand–protein rearrangement to binding kinetics.

P38 belongs to the mitogen-activated protein kinases (MAPKs), a superfamily of enzymes involved in regulating cell functions including proliferation, gene expression, differentiation, and apoptosis.^{15,16} The p38 kinases have four isoforms, p38 α , β , γ , and δ . The major isoform p38 α has been a drug target for treating various inflammatory diseases, including rheumatoid arthritis, asthma, and cardiovascular disease.^{17–21} Like all protein kinases, p38 α has a structurally conserved catalytic domain consisting of two lobes, the N-terminal and C-terminal lobes, which are connected through a flexible hinge region.²² The activation loop includes a DFG (Asp-Phe-Gly) motif, that belongs to the C-terminal lobe but locates outside of the ATP binding pocket. It directly regulates the enzyme activation through its conformational changes, which can be characterized by different orientations of the side chain of Phe from the DFG motif. The active conformation with Phe buried in the α C helix

has DFG-in loop conformations, and the inactive conformation with Phe sterically interfering with ATP binding has DFG-out loop conformations (Figure 1). NMR and computation studies showed the equal population of DFG-in and DFG-out conformations in the apo p38 α .^{23,24} Inhibitors binding to the ATP binding pocket with a DFG-in conformation are usually termed type-I inhibitors.²⁵ Other inhibitors, such as those occupying both the ATP site and a nearby allosteric hydrophobic pocket accessible with DFG-out loop conformations or compounds that bind exclusively within the allosteric pocket are usually termed type-II²⁶ or type-III inhibitors,²⁷ respectively.

Recent advances in computer resources allow for using long-time-scale conventional MD simulations to explore ligand-receptor association and dissociation. However, sampling ligand dissociation pathways can be impractically long, and therefore various computational techniques have been used to investigate dissociation of inhibitors from their binding targets, providing useful information for drug discovery.^{28–36} For example, a recent study with metadynamics and Markov state model cast light on the rate-limiting step of the inhibitor unbinding process from p38 α ,³⁷ and research with umbrella sampling indicated the allosteric channel as the preferred dissociation pathway for type-II and -III inhibitors of p38 α .³⁸ Besides p38 α , different enhanced sampling simulations were used to sample dissociation of inhibitors from kinase family.^{39–49} The adaptive biasing force (ABF) was used to investigate the unbinding process for inhibitors of ALK tyrosine kinase.³⁹ Steered molecular dynamics (MD) simulation was applied to explore the possible dissociation pathways of type-II inhibitor from kinases c-Kit and Abl.^{43,44} Applying biased force as in steered MD and adaptive biasing force simulations is a powerful tool in sampling that can promisingly help drug discovery, but it may also introduce artifacts when sampling dissociation pathways.

Type-I inhibitors target a kinase with a DFG-in loop conformation, which completely exposes the ATP-binding pocket to the solvent; this dissociation pathway is also called the ATP channel. When a type-II or -III inhibitor binds to the allosteric pocket, existing studies suggested another possible dissociation pathway known as the allosteric-pocket channel.³⁸ This study aims to reveal key interactions and possible protein rearrangement that contribute significantly to dissociation energy barrier and rate determination. We applied two enhanced sampling methods, accelerated MD (AMD), and the newly developed pathway search guided by internal motions (PSIM) method to find pathways of ligands, type-I inhibitors SB2 and SK8, type-II inhibitor BIRB796, and type-III inhibitor LIG4, unbinding from p38 α . Then, we used conventional MD simulations for frames selected from the enhanced sampling trajectories to further sample the molecular motions without any biased potential to remove any possible artifacts brought by the enhanced sampling method. As a result, structures of each window from the trajectories for umbrella sampling are nicely overlapped without abrupt conformational movement between two windows. We also ran conventional MD simulations for the free and bound inhibitor-p38 α complexes that serve as references in their two end points. We used umbrella sampling and various postsimulation processing techniques to reveal changes in free energy, molecular rearrangement, and correlations between p38 α and an inhibitor during ligand dissociation. Although the free energy profiles from umbrella sampling cannot represent all possible configuration during unbinding due to insufficient sampling of the complex system, the simulations still allowed us to identify

important molecular interactions and mechanisms that contribute to binding kinetics during ligand unbinding from p38 α . The results also suggest how and why protein rearrangements contribute to slow unbinding processes in BIRB796 and LIG4 and provide information for drug development.

MATERIALS AND METHODS

Molecular Systems

Table 1 lists the structures and experimental data, crystal structure sources, and binding modes of four inhibitors of p38 α ; the inhibitor SB2 binds to both the DFG-in conformation (PDB ID: 1A9U)⁵⁰ and DFG-out conformation (PDB ID: 3GCP).⁵¹ Structures of free DFG-in and DFG-out conformations are from the DFG-in complex (PDB ID: 1A9U) and DFG-out complex (PDB ID: 1W82)⁵² with ligands removed from their crystal structures. The loop region encompassing residues 173–184 in p38 α is not available in the crystal structure 3GCP, and the partial missing loop was modeled by using the loop conformation from the selected frame on MD simulation of free DFG-out protein. BIRB796 binds to PDB ID 1KV2,⁵³ whose missing loop encompassing residues 115–122 and 170–184 was completed with corresponding parts in the crystal structure of 1W82. After replacing the missing loop with a complete loop conformation, a quick 100-step energy minimization was carried out for the substituted loop and its adjacent residues to refine the new loop conformation. The structures of p38 α in complex with SK8 and LIG4 are not available. To model them, we started with structures from PDB IDs 1A9U and 1W82, whose ligands are structurally similar to SK8 and LIG4, respectively. In 1A9U, we modeled SK8 by replacing the 4-methylsulfinylphenyl group of its original ligand with a thiazole analog. In 1W82, we modeled LIG4 by replacing one chlorine atom of its original ligand with a hydrogen atom and adding one methyl group to the benzene ring. Multiple simulations were performed on these systems, as seen in the following subsections, and a summary of simulations with each system is in Table S1.

MD Simulations

We performed conventional MD simulations on five p38 α complexes (SB2 binding to both DFG-in and DFG-out loop conformations) and free p38 α with DFG-in and DFG-out conformations by using the standard simulation package Amber14.⁵⁴ The Amber 99SB force field was used for the protein, and the general Amber force field (gaff) was used for ligands.^{55–58} Although previous studies showed that Amber99 force field may not always provide a good energy balance between helical structures and extended regions of a protein,^{59,60} this force field can result in reasonable structures for the glycine-rich helix and very accurate computed binding free energy for various inhibitors binding to p38 α .²⁴ Therefore, we continued using Amber99SB in this study. The partial charges of ligands were calculated by using the Vcharge program, which is based on electronegativity equalization and fitting electrostatic potentials computed by ab initio quantum calculations.⁶¹ We set up each system as follows. First, the hydrogen, side-chain and whole system were minimized for 500, 5000, and 5000 steps, respectively. An orthorhombic simulation box was then prepared by solvating the systems with a rectangular box of a 12-Å explicit TIP3P water model by the tleap program in Amber14. Each system contains 60,000 – 70,000 atoms. Na⁺ ions were

added as counterions to keep the whole system neutral, and particle mesh Ewald was used to consider long-range electrostatic interactions.⁶² Before equilibration, we minimized waters and the whole system for 10,000 and 20,000 steps, respectively, followed by equilibrium of solvent molecules for 40 ps. Then the systems were gradually heated from 250 K for 20 ps, 275 K for 20 ps, and 300 K for 160 ps. Frames were saved every 1 ps with a time step of 2 fs in the isothermic–isobaric (NPT) ensemble ($T = 300$ K and $P = 1$ atm). We also used the SHAKE procedure to constrain the covalent bonds involving hydrogen atoms during MD simulations.⁶³ Finally, all production runs were performed for no less than 100 ns at 300 K.

Accelerated MD Simulation

AMD uses a bias potential introduced by the McCammon group.⁶⁴ It enhances the conformational sampling of biological systems by adding a continuous non-negative bias boost potential function, $V(r)$, to the potential energy surface when the system potential is below a reference energy, therefore lowering the local barriers and allowing the calculation to advance faster.

The AMD modification of the potential is defined by the following equation:

$$V^*(r) = V(r) + \Delta V(r)$$

$$\Delta V(r) = \begin{cases} 0, & V(r) \geq E \\ \frac{(E - V(r))^2}{\alpha + (E - V(r))}, & V(r) < E \end{cases}$$

where $V(r)$ is the original potential, E is the reference energy, and $V^*(r)$ is the modified potential. $V(r)$ is the boost potential, and α is the acceleration factor. The potential energy surface is flattened as the acceleration factor α decreases, making it easier to cross energy barriers between local minimas.

The boost potential $V(r)$ can be further divided into potential-boost and dihedral-boost.

$$\Delta V(r) = \frac{(E_p - V(r))^2}{(\alpha P + E_p - V(r))} + \frac{(E_d - V_d(r))^2}{(\alpha D + E_d - V_d(r))}$$

It allows for boosting independently only the torsional terms of the potential with input parameters (E_d , αD), the whole potential at once (E_p , αP), or the whole potential with an extra boost to the torsions.

For simulations of p38 α , we applied both potential-boost and dihedral-boost. The input parameters take the following form:

$$E_d = V_{d_avg} + 4N_{residues}$$

$$\alpha D = 0.8 N_{\text{residues}}$$

$$E_p = V_{p_avg} + 0.2 N_{\text{atoms}}$$

$$\alpha P = 0.2 N_{\text{atoms}}$$

where N_{atoms} and N_{residues} are the total number of atoms and total number of residues of solute, V_{d_avg} and V_{p_avg} are the average dihedral and total potential energies, respectively, calculated from 100 ns conventional MD simulations. For a higher acceleration, we added another $3 \times \alpha D$ to E_d .

Pathway Search Guided by Internal Motions (PSIM)

PSIM is an enhanced conformational search method specifically designed for search of dissociation pathways of ligand–receptor systems.⁶⁵ It presents atomistic motions of a ligand–protein bound complex along internal principal component (PC) modes obtained by classical MD simulations. Although the ligand always stayed in the binding pocket of p38 α , PC modes describe natural motion of the system and are used by PSIM to guide ligand dissociation. To overcome problems with Cartesian and classical internal coordinates (Z -matrix) that show problem in smoothly presenting dihedral rotation or generating nonphysical distortions, PSIM uses new multilayer internal coordinates and trigonometric functions to correctly present protein motions by using dihedral rotations. In brief, the multilayer internal coordinates divide a protein into N fragments, shown in Figure S1, with each fragment presented by the internal coordinates, and the fragments are connected to present an entire molecule. By distorting the system with these three-dimensional motions along selected internal PC modes, PSIM performs systematic searches for the dissociation pathways and accepts and rejects new conformations by using geometric criteria rather than energy evaluation or minimization. To ensure reasonable conformations, short minimization on bond and angle terms is performed periodically in addition to the simple geometric criteria. To speed up searches for unbinding pathways, we did not include the whole protein when constructing the internal PC modes, and the selected backbone and side chain dihedrals are listed in the Supporting Information (SI). The selection resulted in 739 PC modes, and all modes were used for conformational search. We used the initial structure of the MD simulation to begin our search, but any randomly chosen frames from a MD simulation can serve as an initial conformation for PSIM. The output step number was set to 1000, with the distortion step size equal to 5% of the eigenvector of each internal PC mode. The workflow of the search is illustrated in Figure S2, and except the numbers mentioned above, we used the default values for other parameters during the search. Starting from the initial structure, we performed the PSIM search and repeated it for multiple iterations. We manually chose conformations from an existing search to start a new iteration until a ligand dissociated from the binding site. We repeated this procedure and performed 3 – 16

iterations to obtain dissociation pathways; therefore, the dissociation pathway is a collection of multiple trajectories obtained from each iteration.

Construction of Potential of Mean Force (PMF)

Umbrella sampling was used to compute the free energy along the dissociation pathway. By adding multiple overlapping biasing potentials along the dissociation pathway as the reaction coordinate (RC), umbrella sampling can sufficiently sample all points on the RC. First, the whole RC is divided into a series of continuous windows, then a harmonic biased potential is applied to add on the original potential in each window. The equation for the harmonic potential is shown below:

$$u_i = k_i(r - r_i)^2$$

where u_i is the biased potential in window i , r is the current position of RC, r_i is the reference position in window i , and k_i is the force constant used to restrain the biased molecule in the biased potential. Here, a force constant of 5 kcal/mol·Å² was used in all umbrella sampling (US) simulation windows. WHAM was used to construct the free energy profile along the RC.^{66,67}

Here, the RC was separated into bins with 0.2-Å width for the WHAM calculation after each umbrella sampling window. The tolerance for iteration was set to 0.0001 to obtain convergent free energy plots. The temperature was set to 300 K to remain consistent with the simulation temperature. The distance between C α of Arg73 and CC2 of SB2 (CC2 of SK8) was selected as the RC. For BIRB-796 and LIG4, two sets of RCs were selected. The distance between C α of Met109 and C3 of BIRB796 (C7 of LIG4) was selected as the RC for the allosteric pathway, and the distance between C α of Arg73 and C3 of BIRB796 (C12 of LIG4) was selected as the RC for the ATP pathway. Each set of the simulations contains simulation windows with 0.25-Å length for each. For each window, a 10 ns MD simulation was performed for a selected structure postprocessed from our search with AMD or PSIM with postprocessing.

Although AMD and PSIM provided dissociation pathways, the frames saved were not continuous enough to smoothly connect each window, which is only 0.25 Å apart from each other. Therefore, we selected frames from AMD or PSIM trajectories along the RC as an initial structure to run multiple short 10 ns conventional MD simulations and saved a frame every 1 ps. In most simulations, a ligand stayed in that position; however, in some cases, the ligand moved toward inside or outside the cavity. As a result, we could build a smooth dissociation pathway using the overlapped conformations obtained from two to three 10 ns MD simulations. To quantify overlapping, we measured the root-mean-square deviation (RMSD) value for different 10 ns MD frames of a ligand, and the frames with the smallest RMSD but 0.25 Å apart along the RC were selected as initial structures for each umbrella sampling window. An example for reconstruction of a dissociation path with short 10 ns MD simulations for SB2 unbinding from p38 α with the DFG-in conformation is shown in Figure S3. Notably, for the complex ligand–protein dissociation pathways, selecting one or a few degrees of freedom as an RC simplified the intermolecular attractions and concerted

conformational changes. As a result, although plots can reveal important changes in conformations and inter molecular interactions, we did not anticipate that the computed PMF depth accurately reflects the absolute binding free energy G .

Post-MD Analysis

Correlation between different parts of p38 α was analyzed by using T-Analyst.⁶⁸ We first calculated correlations between backbone dihedrals (Phi and Psi angles) of each residue of protein as well as rotatable dihedral angles of ligands (Table 1) to examine the correlation. Because the entire p38 α has hundreds of backbone dihedrals, to simplify the correlation map, we divided p38 α into different subgroups based on its secondary structure and summed the absolute values of correlation within each subgroup. Therefore, the output correlation maps show correlation between different subgroups of protein (ie, correlation between the α C helix and the activation loop). It is worth mentioning that conformations sampled by both aMD and PSIM were examined carefully by comparing their conformations with those sampled by conventional MD simulations. All the trajectories were inspected to ensure that the enhanced sampling methods maintained reasonable secondary structures and loop stretch during ligand unbinding.

RESULTS AND DISCUSSION

We used AMD simulations of five complex systems to study their dissociation pathways. However, only type-I inhibitors, SB2 and SK8, successfully dissociated in high-boost AMD, whereas the type-II inhibitor BIRB796 and type-III inhibitor LIG4 barely deviated from their binding position. Therefore, we also used PSIM, a pathway search method based on internal PC modes, to successfully sample dissociation pathways for all the ligands, including BIRB796 and LIG4. The initial loop structures for BIRB796 and LIG4 are in the DFG-out form, so both allosteric and ATP pathways were sampled with PSIM. After we obtained the dissociation pathways for all ligands that left the binding pocket, umbrella sampling was used to illustrate the free energy profile along the dissociation processes and key interactions that contribute to the free energy changes during unbinding. Use of positions of a ligand relative to p38 α as a reaction coordinate in umbrella sampling missed important information of protein rearrangement when investigating binding kinetics. We analyzed the ligand-protein correlation during the dissociation process and identified protein hinge motion as a major movement as well. Therefore, we accessed the protein rearrangement guided by the protein hinge motion during ligand dissociation and revealed significantly different levels of energetically required protein motions between type-I and type-II/III inhibitors.

To serve as our references, we ran 100 ns conventional MD for the free p38 α with DFG-in and DFG-out loop conformations and performed correlation analysis in comparison with their ligand-bound states. We also ran 650 ns conventional MD for the SB2 (bound with DFG-in loop) and BIRB796 complexes. With k_{off} values ranging from 8.3×10^{-6} to 7.7 s^{-1} in our p38 α systems, the dissociation time ranged from 0.1 to $>10^5$ s. As a result, no ligand dissociation should be observed during the simulations.

Dissociation Pathways of Type-I Inhibitors, SB2 and SK8

Figure 2 illustrates key interactions between SB2 bound to p38 α with a DFG-in loop conformation, in which the attractions should be broken or loosened before or during the dissociation process. For example, there are two hydrogen bonds between the pyridine ring N and backbone nitrogen of Met109 and the N3 atom of the imidazole ring and Lys53, and the phenyl ring of 4-methylsulfinylphenyl group forms a stacking interaction with Tyr35 (Figure 2). In addition to these key interactions, SB2 bound to the DFG-out loop conformation has an additional stacking interaction between the phenyl ring and Phe169 of the DFG-motif. We first used high- or low-boost AMD for sampling and examined the advantage for sampling, as detailed in SI section 1. AMD with high boost and the PSIM method successfully sampled dissociation pathways for SK8 bound to the DFG-in conformation and SB2 bound to both DFG-in and DFG-out conformations.

Both AMD and PSIM found the same key interactions between SB2/SK8 and p38 α which are required to break in order to unbind the ligand from the pocket (Figures 3, S6, S7, S8, S9, and S10). Using the dissociation pathways sampled by AMD, umbrella sampling along the pathway was used to construct a free energy plot to further explore free energy changes associated with ligand unbinding. First the hydrogen bond between SB2 and Lys53 breaks (Figure 3A), followed by the motion of the 4-methylsulfinylphenyl group (Figure 3B). Then the second hydrogen bond between pyridine nitrogen and Met109 breaks (Figure 3C), and finally, the ligand is outside the edge of the binding cavity (Figure 3D) and eventually diffuses away. As for SB2 unbinding from p38 α with a DFG-in conformation, the two other systems both dissociate along the ATP channel. Their free energy plots are also similar (Figure S7, S9 compared to Figure 3) and the PSIM pathways are the same as found by AMD (Figures S8, S10). The free energy continues to increase during dissociation, but no significant energy barriers were observed during the unbinding process.

Previous studies showed that water effects can be important in ligand binding kinetics.^{69–72} Therefore, we investigated the presence of bridge water molecules with long residence time and also counted the average number and the fluctuation using the standard deviation of pocket-water molecules in the binding site of the protein during SB2 unbinding from p38 α with a DFG-in conformation (Figure S11). It is worth noting that in addition to pocket-water occupancy, the water-density fluctuations in the binding site and surface of a protein may also significantly contribute to drug unbinding.^{69,73} Figure S11 shows a rapid increase in number of pocket-waters when p38 α moved to a position shown in Figure 3B, where the motion of a 4-methylsulfinylphenyl group created space for resolvating water molecules. However, the number of pocket-waters fluctuated considerably. Unlike ligands binding to HIV protease, in which a few transient water molecules stay for a long time between the ligand and protein,⁷⁴ with SB2 unbinding from p38 α , all the water molecules were replaced by each other frequently. However, a water molecule can still weaken interactions between functional groups of SB2 and the protein, which assists the unbinding process. The pocket-water fluctuations shown in our simulations are worth further investigation using passage time theory, density profile, or free energy landscape to reveal the transitions between locally wet and dry regions that may deepen our understanding on unbinding kinetics.^{75–77}

In addition, different water models may slightly influence protein and ligand dynamics, which may have an effect on modeling binding kinetics as well.⁷⁸

Dissociation Pathways of a Type-II Inhibitor, BIRB796, and Type-III Inhibitor, LIG4, Sampled by PSIM

Although high-boost AMD successfully simulated dissociation pathways for the type-I inhibitors SB2 and SK8, the method could not sample ligand dissociation for type-II or type-III inhibitors. Experimentally, the ligands have much longer residence time: 625 s for LIG4 and 1.2×10^5 s for BIRB796. Therefore, we applied the newly developed PSIM method to sample the dissociation pathways for BIRB796 and LIG4.

Complex conformations from conventional MD and crystal structures for BIRB796 and LIG4 complexes with p38 α show that urea forms two hydrogen bonds between the urea NH group and Glu71 in the N-terminal lobe and between the urea CO group and Asp168 backbone nitrogen in the C-terminal lobe (Figure 4). The two hydrogen bonds clamp ligands BIRB796 and LIG4 within the cleft. In addition, an extended morpholino substituent forms a hydrogen bond with a backbone nitrogen of Met109. To dissociate a ligand, trajectories obtained from PSIM showed that the cleft needed to open, which also associated with the protein hinge motion between the two lobes. The opening allows BIRB796 and LIG4 to unbind directly from the allosteric pocket (SI Movie 2) or move further toward the ATP binding site and dissociate from there (SI Movie 1). The latter pathway is similar to the unbinding pathways sampled for type-I inhibitors.

First we examined the free energy profile constructed from BIRB796 unbinding from the allosteric pocket. Figure 5A shows that two hydrogen bonds between the urea group of BIRB796 and Glu71 and Asp168 need to break, and the extended morpholino substituent rotates along the opened cleft, breaking another hydrogen bond with Met109. The free energy increases ~ 2 kcal/mol. The free energy continues to increase as BIRB796 wiggles out along the activation loop to the edge of binding cavity (Figure 5B), where His174 forms a stacking interaction with the naphthalene group of BIRB796. The activation loop then rearranges and fluctuates in concert with the ligand to unbind the ligand, which results in decreasing free energy from 5.5 to 3.4 kcal/mol (Figure 5C). BIRB796 finally breaks the stacking interaction with His174 and moves away (Figure 5D). PSIM found four unbinding trajectory from the allosteric pocket; although only one of the trajectory was used to construct PMF, others all have important formation and breakage of interactions, such as contacting with His174 after breaking hydrogen bonds between BIRB796 and Glu71/Asp168 (Figure S12).

For BIRB796 dissociating from the ATP pocket, the dissociation of BIRB796 also starts with cleft opening, extended morpholino substituent rotating, accompanied by hydrogen bond breaking. The large *5-tert-butyl-2-p-tolyl-2H*-pyrazol group rotates and moves toward the ATP pocket, whereas Phe169 starts to form a stacking interaction with the naphthalene group of BIRB796 (Figure 6A). This path is not energetically favorable, and the free energy barrier rapidly increases to 10 kcal/mol. Then BIRB796 starts to dissociate from the ATP pocket, similar to other type-I ligands. The free energy continues to increase to 16.8 kcal/mol until the stacking interaction between BIRB796 and Phe169 is loosened (Figure

6B). The glycine-rich loop needs to slightly lift up to create room for BIRB796 to continue unbinding from the cavity (Figure 6C). Once BIRB796 moves out of the cavity, the glycine-rich loop returns to its original position (Figure 6D). Similar changes in interactions shown in the PMF plots for LIG4 are in Figures S13 and S14.

Although the absolute binding free energies in a one-dimensional free energy profile cannot accurately reproduce the ligand-p38 α binding free energy (ΔG) and the barriers, the free energy plots can distinguish that BIRB796 and LIG4 prefer to dissociate from the allosteric pathway instead of moving to the ATP pocket and dissociating from there. Our results regarding the preferred binding path through the allosteric channel and the opening of the binding pockets agree with a recent computational study of type-II/III ligand unbinding from p38 α .³⁸ PSIM only found one dissociation path from the ATP binding site for type-II/III inhibitors. Because PSIM prefers using guidance by low-frequency PC motions for pathway search, it is unsurprising that the method is less efficient to find pathways with high free energy barriers. Our simulation is consistent with a recent paper;³⁸ thus, we did not use PSIM to keep searching more high-barrier dissociation pathways from the ATP binding site. Notably, the free energy plots only consider one chosen degree of freedom, which inevitably simplifies and smooths out the free energy barriers. Because we observed noticeable protein motions during ligand dissociation, we performed further analysis to reveal the protein dynamics and used the information for another coordinate to investigate the unbinding free energy barriers.

We also examined the changes in number of pocket-water molecules during BIRB796 dissociation. Figure S15 shows a rapid increase in number of pocket-waters when the cleft between the N- and C-terminal lobes opens (Figures 5A and 6A). During ligand dissociation processes, the number of pocket-waters plateaus and seven water molecules, on average, are in the pocket, similar to that during SB2 dissociation. As for the fast binding molecules SB2 and SK8, the number of pocket-waters greatly fluctuated and the water molecules were constantly replaced by each other. As a result, even though the resolution process is important for unbinding, this process is less likely to contribute significantly to distinguishing slow BIRB796 and fast SB2 unbinding.

Principal Component Analysis (PCA) and Correlation Analysis

To obtain the major motion of protein, we first performed PCA for trajectories from conventional MD (Table S1) to check the first PC motion of free p38 α with DFG-in or DFG-out conformations (Figure S16). Note that we carried out multiple conventional MD runs and they all showed the same major PC motions. However, due to space limit, we only report results of PC motions from one MD result here. To more clearly elucidate the protein motions, we grouped residues based on its secondary structure (Figure 7); free p38 α showed strong correlation between the hinge region (L9 loop, α D helix, L10 loop) and two lobes (N- and C-terminal lobes) despite the loop conformation. The protein with the DFG-out loop conformation showed slightly stronger correlation (Figures S16 and S17), presumably due to larger fluctuations in hinge regions, which is consistent with the root-mean-square fluctuation (RMSF) plot (Figure S18). Figure S19 shows that p38 α complexes retain strong correlation in the hinge region, as detailed in SI section 2. The differences in protein

conformational correlation are more substantial when SB2 and BIRB796 are unbinding from p38 α with DFG-in and DFG-out conformations, respectively (Table S1, Figure 8). When SB2 is in the middle of dissociation pathway, p38 α and SB2 mostly correlated solely within hinge region and the activation loop. In contrast, during the dissociation of BIRB796, we see strong correlation around the hinge region and activation loop and also with the upper arm of the hinge in the N-terminal lobe (L3 loop, β 2 sheet, and β 3 sheet), which suggests that p38 α encounters more sizable rearrangement during BIRB796 unbinding.

Role of Protein Hinge Motion during Inhibitor Dissociation

To quantify the contribution of protein rearrangement to free energy barriers, we selected another coordinate based on PCA and correlation maps to present protein motion, to construct another plot for a one-dimensional free energy profile. Notably, although two-dimensional (2-D) umbrella sampling can be used to construct 2-D free energy plots, we found that viewing and examining free energy barriers versus protein rearrangement is difficult with the 2-D free energy plots. We used the distance between C α of Glu71 and Asp168 and C α of Val30 and Ala111 as a coordinate to represent hinge motions during ligand dissociation. For all pyrazolourea compound analogs such as the BIRB796 and LIG4 complex with a DFG-out conformation of p38 α , a polar channel formed by Glu71 and Asp168 is conserved and reported to be very important. For type-I inhibitors, Val30 and Ala111 are in the unbinding pathways when type-I ligands are unbinding from the ATP binding site with a DFG-in protein conformation (Figure 9).

Figure 10 shows the free energy change during the hinge movement while BIRB796 is located in the crystal structure bound form, middle of the dissociation pathway, right outside the binding cavity and completely dissociated from p38 α with a DFG-out conformation. When an inhibitor is far from the protein binding site, the protein motion can be presented by a shallow energy well with the equilibrium position located at 11.1 Å of the coordinate (hinge distance between Glu71 and Asp168). Interestingly, when BIRB796 is in the binding cavity, the equilibrium position shifts to 10.1 Å and the free energy well narrows. Within thermal fluctuation RT (\sim 0.6 kcal/mol), the hinge distance can move less than 1 Å, for much more rigid complex structure. Because BIRB796 dissociates in a position shown in Figure 5A with the opening cleft, the equilibrium hinge distance increases to 11.9 Å. It needs 2.6 kcal/mol to widen the hinge distance from 10.1 to 11.9 Å. The large energy barrier from the protein rearrangement explains the slow dissociation rate of BIRB796 and has been reported recently for slow ligand binding to tyrosine kinases due to the induced fit/protein rearrangement.⁷⁹ Notably, when BIRB796 locates just outside the cavity, the equilibrium position of the hinge distance is the same as when BIRB796 is far from p38 α . However, the existence of a ligand near the binding pocket perturbs p38 α fluctuation of N- and C-terminal lobes, thereby narrowing the energy well for the hinge motion. Similar to BIRB796, LIG4 requires remarkable cleft opening and increases energy barriers for ligand dissociation (Figure S20).

For type-I ligand SB2 (bound with the DFG-in loop conformation), the equilibrium hinge distances are highly similar, regardless of where SB2 locates (Figure 11), which suggests that the protein hinge movement contributes insignificantly to the dissociation energy

barrier. The bound SB2 slightly rigidifies the p38 α movement and results in a narrower energy well. However, unbinding of SB2 from the pocket (Figure 3A) does not disturb protein fluctuation, and p38 α can fluctuate as if no SB2 is present, which suggests that protein rearrangement does not contribute to the unbinding free energy barriers. The shallow energy well also suggests that it is easier for SB2 (DFG-in) to move out of the cleft. Similar to the SB2 bound complex with a DFG-in conformation, during dissociation of SB2 bound with a DFG-out conformation and SK8, the equilibrium hinge distance is close to that when p38 α is free and in complex with a ligand, as shown in Figure S21. It is nearly barrier free for the hinge to move. On comparing the crystal structures when SB2 was bound to a DFG-in or DFG-out conformation, the average equilibrium hinge distance between residues Val30 and Ala111 is 12 Å in SB2 (DFG-in) or 15 Å, respectively. The cleft may need to open up as the DFG motif flips from a DFG-in to DFG-out conformation. However, because of the location of SB2 bound to p38 α , no energetically protein motions are required for either loop conformations during SB2 dissociation.

To ensure that the results of free energy calculation during hinge movement do not depend on the choice of coordinates, we also constructed free energy plots using the hinge distance between Val30 and Ala111 of p38 α for BIRB796 and confirmed high free energy cost for hinge opening with BIRB796 dissociation with a different set of coordinate. Similarly, we plotted the free energy changes during hinge movement by using the distance between Glu71 and Asp168 for SB2 (bound with DFG-in loop). Figure 12 confirmed that the opening cleft during SB2 dissociation does not increase free energy, which again suggests that SB2 does not require expensive conformational rearrangement of p38 α , thereby resulting in a faster kinetics.

Since protein conformational rearrangement plays a crucial role in dissociation of type-II/III ligands, we designed a mutation associated with the flexibility of the hinge region to examine the changes in binding kinetics. We hypothesized that a more barrier-free hinge motion can lead to faster dissociation of type-II/III ligands. To confirm this, we mutated Tyr69 in the α C helix, Phe327 in the L16 loop and Trp337 in the L16 helix into glycine and performed a 100 ns conventional MD simulation for BIRB796 bound with mutated p38 α with a DFG-out conformation. Before mutation, Tyr69, Phe327, and Trp337 form a stacking interaction with each other and can mutually stabilize the L16 loop, α L16 helix, and α C helix. After mutation, the L16 loop is much more flexible without the stacking interaction, and both the α L16 and α C helix shift up. Even though the average hinge distance does not change much due to the concerted shifting up for the activation loop (Figure 13), conventional MD showed that the mutation was more flexible, and the average RMSD of backbone atoms of the α C helix increased from 1.0 to 1.7 Å after mutation. On comparing free energy change during the hinge movement with protein mutation, the energy well become shallower than those computed for the wild-type p38, especially when BIRB796 is in the crystal structure bound form and middle of the dissociation pathway. The equilibrium hinge distance needed for BIRB796 dissociation is significantly closer to that in the crystal structure. As a result, the energy cost due to protein motion for dissociating BRIB796 can be largely reduced (Figure 14). The computation experiment demonstrates the importance of flexibility of the hinge region, which agrees with experimental data that mutations of Tyr69,

Phe327, and Trp337 in p38 α can result in disordered enzyme activation⁸⁰ and suggests a new direction for future kinase activity study and inhibitor design.

CONCLUSION

In this study, we examine the detailed protein–ligand interactions that contribute to dissociation free-energy cost for type-I, -II, and -III inhibitors, SB2 and SK8, BRIB796, and LIG4, respectively, unbinding from p38 α . We focus on revealing important features such as breaking key intermolecular interactions between a ligand and residues in the pockets and molecular rearrangements that contribute significantly to rate determination for different types of ligands. We used AMD and PSIM to first sample dissociation pathways for each inhibitor and to reveal the molecular motions during ligand dissociation. Guided by the frames along the unbinding pathways, umbrella sampling was used to construct free energy plots to illustrate correlations between free energy changes and transitions of molecular conformations. It is worth mentioning that PSIM uses internal PC modes to guide the search for dissociation pathways which has advantages over simulation-based methods for molecular systems with slow noncovalent kinetic behavior. The search method may produce rapid conformational movement; therefore, short conventional MD runs can be applied for selected frames to further smooth the molecular motions.

Although the depths of free energy plots cannot accurately rank inhibitor-binding free energy to p38 α (G), the plots can distinguish favorable and unfavorable dissociation pathways from the depths. AMD and PSIM found one preferred unbinding pathway via the ATP channel for inhibitors SB2 and SK8, whereas PSIM found two dissociation pathways via both ATP and allosteric channels for BRIB796 and LIG4. The free energy plots further show that the allosteric channel is the major unbinding pathway for the two inhibitors. We found that because of the molecular properties of the binding pocket and the tight binding inhibitors studied here, inhibitors must break important and conserved intermolecular interactions which results in one major dissociation direction when a ligand is leaving the pocket. Although the free energy profiles from umbrella sampling cannot represent all possible configuration during unbinding due to insufficient sampling of the complex system, the simulations still allowed us to identify important molecular interactions and mechanisms that contribute to binding kinetics during ligand unbinding from p38 α . Correlation analysis suggested that the hinge motion may play an important role in ligand dissociation. The free energy changes during hinge movement of the protein confirm the large free energy cost of hinge movement when unbinding type-II/III inhibitors, which explains their slow dissociation rate as compared with type-I ligands, whose dissociation processes does not require large free energy barriers. Therefore, we computationally mutated residues to reduce free energy cost for protein rearrangement, and the simulation suggested that a more flexible hinge region may facilitate the entry/exit of type-II/III ligands.

The success of the combination of AMD and PSIM simulations and free energy plots of the dissociation of different types of p38 α inhibitors reveals detailed protein–ligand interactions as well as protein conformational rearrangements during ligand dissociation. This study illustrated that when inhibitors unbind/bind to DFG-out loop conformations of p38 α kinase, the protein must undergo an unfavorable and transient conformation that is not required

when inhibitors unbind/bind to DFG-in loop conformations. This temporary rearrangement creates a few kilocalories per mole energy barrier, resulting in slower binding/unbinding kinetics. This indicates that inhibitors binding to either of the loop conformations have intrinsic limitations due to protein motion, and drug development may need to target only one of the protein binding pockets, depending on whether slow or fast kinetic binding is desired. If there is no significant energy barrier raised by protein rearrangement, then the drug development project can concentrate on solvent effect and ligand-protein binding free energy, as described in other publications.^{69–73} In addition, the computation provides powerful tools and useful guidance for future study of binding/unbinding mechanisms of kinase systems and inhibitor development.

Supplementary Material

Refer to Web version on PubMed Central for supplementary material.

Acknowledgments

This study was supported by the US National Institutes of Health (GM-109045), and National Science Foundation national supercomputer centers (TG-CHE130009). We thank Dr. Zhiye Tang for helping to run the PSIM method.

References

1. Cohen P. Protein Kinases—The Major Drug Targets of the Twenty-First Century? *Nat Rev Drug Discovery*. 2002; 1:309–315. [PubMed: 12120282]
2. Laufer, S., Bauer, S. *Methods in Molecular Biology 795: Kinase Inhibitors: Methods and Protocols*. In: Bernhard, Kuster, editor. ChemBioChem. Vol. 13. 2012. p. 2146–2146.
3. Margutti S, Laufer SA. Are MAP Kinases Drug Targets? Yes, but Difficult Ones. *ChemMedChem*. 2007; 2:1116–1140. [PubMed: 17541990]
4. Sawyers C. Targeted Cancer Therapy. *Nature*. 2004; 432:294–297. [PubMed: 15549090]
5. Wu P, Nielsen TE, Clausen MH. Small-Molecule Kinase Inhibitors: an Analysis of FDA-Approved Drugs. *Drug Discovery Today*. 2016; 21:5–10. [PubMed: 26210956]
6. Copeland RA, Pompliano DL, Meek TD. Drug-Target Residence Time and Its Implications for Lead Optimization. *Nat Rev Drug Discovery*. 2006; 5:730–739. [PubMed: 16888652]
7. de Witte WE, Danhof M, van der Graaf PH, de Lange EC. In Vivo Target Residence Time and Kinetic Selectivity: The Association Rate Constant as Determinant. *Trends Pharmacol Sci*. 2016; 37:831–842. [PubMed: 27394919]
8. Pan AC, Borhani DW, Dror RO, Shaw DE. Molecular Determinants of Drug-Receptor Binding Kinetics. *Drug Discovery Today*. 2013; 18:667–673. [PubMed: 23454741]
9. Schuetz DA, de Witte WEA, Wong YC, Knasmueller B, Richter L, Kokh DB, Sadiq SK, Bosma R, Nederpelt I, Heitman LH, Segala E, Amaral M, Guo D, Andres D, Georgi V, Stoddart LA, Hill S, Cooke RM, De Graaf C, Leurs R, Frech M, Wade RC, de Lange ECM, Ijzerman IJ, Muller-Fahnow A, Ecker GF. Kinetics for Drug Discovery: An Industry-Driven Effort to Target Drug Residence Time. *Drug Discovery Today*. 2017; 22:896–911. [PubMed: 28412474]
10. Wentsch HK, Walter NM, Bührmann M, Mayer-Wrangowski S, Rauh D, Zaman GJR, Willemsen-Seegers N, Buijsman RC, Henning M, Dauch D, Zender L, Laufer S. Optimized Target Residence Time: Type II/2 Inhibitors for P38 α MAP Kinase with Improved Binding Kinetics through Direct Interaction with the R-Spine. *Angew Chem, Int Ed*. 2017; 56:5363–5367.
11. Chiu SH, Xie L. Toward High-Throughput Predictive Modeling of Protein Binding/Unbinding Kinetics. *J Chem Inf Model*. 2016; 56:1164–1174. [PubMed: 27159844]
12. Ferruz N, De Fabritiis G. Binding Kinetics in Drug Discovery. *Mol Inf*. 2016; 35:216–226.

13. Tiwary P, Limongelli V, Salvalaglio M, Parrinello M. Kinetics of Protein–Ligand Unbinding: Predicting Pathways, Rates, and Rate-Limiting Steps. *Proc Natl Acad Sci U S A*. 2015; 112:E386–E391. [PubMed: 25605901]
14. Zheng X, Wang J. The Universal Statistical Distributions of the Affinity, Equilibrium Constants, Kinetics and Specificity in Biomolecular Recognition. *PLoS Comput Biol*. 2015; 11:e1004212. [PubMed: 25885453]
15. Adams JL, Badger AM, Kumar S, Lee JC. P38 MAP Kinase: Molecular Target for the Inhibition of Pro-inflammatory Cytokines. *Prog Med Chem*. 2001; 38:1–60. [PubMed: 11774793]
16. Cuenda A, Rousseau S. P38 MAP-Kinases Pathway Regulation, Function and Role in Human Diseases. *Biochim Biophys Acta, Mol Cell Res*. 2007; 1773:1358–1375.
17. Buhler S, Laufer SA. P38 MAPK Inhibitors: A Patent Review (2012–2013). *Expert Opin Ther Pat*. 2014; 24:535–554. [PubMed: 24611721]
18. Gupta J, Nebreda AR. Roles of P38 α Mitogen-Activated Protein Kinase in Mouse Models of Inflammatory Diseases and Cancer. *FEBS J*. 2015; 282:1841–1857. [PubMed: 25728574]
19. Igea A, Nebreda AR. The Stress Kinase P38 α as a Target for Cancer Therapy. *Cancer Res*. 2015; 75:3997–4002. [PubMed: 26377941]
20. Kumar S, Boehm J, Lee JC. P38 MAP Kinases: Key Signalling Molecules as Therapeutic Targets for Inflammatory Diseases. *Nat Rev Drug Discovery*. 2003; 2:717–726. [PubMed: 12951578]
21. Martin ED, Bassi R, Marber MS. P38 MAPK in Cardioprotection – Are We There yet? *Br J Pharmacol*. 2015; 172:2101–2113. [PubMed: 25204838]
22. Huse M, Kuriyan J. The Conformational Plasticity of Protein Kinases. *Cell*. 2002; 109:275–282. [PubMed: 12015977]
23. Vogtherr M, Saxena K, Hoelder S, Grimme S, Betz M, Schieberr U, Pescatore B, Robin M, Delarbre L, Langer T, Wendt KU, Schwalbe H. NMR Characterization of Kinase P38 Dynamics in Free and Ligand-Bound Forms. *Angew Chem, Int Ed*. 2006; 45:993–997.
24. Huang YM, Chen W, Potter MJ, Chang CE. Insights from Free-Energy Calculations: Protein Conformational Equilibrium, Driving Forces, and Ligand-Binding Modes. *Biophys J*. 2012; 103:342–351. [PubMed: 22853912]
25. Wilson KP, McCaffrey PG, Hsiao K, Pazhanisamy S, Galullo V, Bemis GW, Fitzgibbon MJ, Caron PR, Murcko MA, Su MS. The Structural Basis for the Specificity of Pyridinylimidazole Inhibitors of P38 MAP Kinase. *Chem Biol*. 1997; 4:423–431. [PubMed: 9224565]
26. Kufareva I, Abagyan R. Type-II Kinase Inhibitor Docking, Screening, and Profiling Using Modified Structures of Active Kinase States. *J Med Chem*. 2008; 51:7921–7932. [PubMed: 19053777]
27. Simard JR, Getlik M, Grutter C, Schneider R, Wulfert S, Rauh D. Fluorophore Labeling of the Glycine-Rich Loop as a Method of Identifying Inhibitors that Bind to Active and Inactive Kinase Conformations. *J Am Chem Soc*. 2010; 132:4152–4160. [PubMed: 20201574]
28. Dickson A, Lotz SD. Ligand Release Pathways Obtained with WExplore: Residence Times and Mechanisms. *J Phys Chem B*. 2016; 120:5377–5385. [PubMed: 27231969]
29. Lovera S, Morando M, Pucheta-Martinez E, Martinez-Torrecedrera JL, Saladino G, Gervasio FL. Towards a Molecular Understanding of the Link between Imatinib Resistance and Kinase Conformational Dynamics. *PLoS Comput Biol*. 2015; 11:e1004578. [PubMed: 26606374]
30. Saladino G, Gauthier L, Bianciotto M, Gervasio FL. Assessing the Performance of Metadynamics and Path Variables in Predicting the Binding Free Energies of P38 Inhibitors. *J Chem Theory Comput*. 2012; 8:1165–1170. [PubMed: 26596735]
31. Sun H, Li Y, Shen M, Li D, Kang Y, Hou T. Characterizing Drug–Target Residence Time with Metadynamics: How to Achieve Dissociation Rate Efficiently without Losing Accuracy against Time-Consuming Approaches. *J Chem Inf Model*. 2017; 57:1895–1906. [PubMed: 28749138]
32. Tiwary P. Molecular Determinants and Bottlenecks in the Dissociation Dynamics of Biotin–Streptavidin. *J Phys Chem B*. 2017; 121:10841–10849. [PubMed: 29117680]
33. Wang Y, Martins JM, Lindorff-Larsen K. Biomolecular Conformational Changes and Ligand Binding: From Kinetics to Thermodynamics. *Chem Sci*. 2017; 8:6466–6473. [PubMed: 29619200]
34. De Vivo M, Masetti M, Bottegoni G, Cavalli A. Role of Molecular Dynamics and Related Methods in Drug Discovery. *J Med Chem*. 2016; 59:4035–4061. [PubMed: 26807648]

35. Mollica L, Theret I, Antoine M, Perron-Sierra F, Charton Y, Fourquez JM, Wierzbicki M, Boutin JA, Ferry G, Decherchi S, Bottegoni G, Ducrot P, Cavalli A. Molecular Dynamics Simulations and Kinetic Measurements to Estimate and Predict Protein-Ligand Residence Times. *J Med Chem.* 2016; 59:7167–7176. [PubMed: 27391254]
36. Mollica L, Decherchi S, Zia SR, Gaspari R, Cavalli A, Rocchia W. Kinetics of Protein-Ligand Unbinding via Smoothed Potential Molecular Dynamics Simulations. *Sci Rep.* 2016; 6:25299. [PubMed: 27151769]
37. Casanovas R, Limongelli V, Tiwary P, Carloni P, Parrinello M. Unbinding Kinetics of a P38 MAP Kinase Type II Inhibitor from Metadynamics Simulations. *J Am Chem Soc.* 2017; 139:4780–4788. [PubMed: 28290199]
38. Sun H, Tian S, Zhou S, Li Y, Li D, Xu L, Shen M, Pan P, Hou T. Revealing the Favorable Dissociation Pathway of Type II Kinase Inhibitors via Enhanced Sampling Simulations and Two-End-State Calculations. *Sci Rep.* 2015; 5:8457. [PubMed: 25678308]
39. Sun H, Li Y, Li D, Hou T. Insight into Crizotinib Resistance Mechanisms Caused by Three Mutations in ALK Tyrosine Kinase Using Free Energy Calculation Approaches. *J Chem Inf Model.* 2013; 53:2376–2389. [PubMed: 23952683]
40. Meng Y, Pond MP, Roux B. Tyrosine Kinase Activation and Conformational Flexibility: Lessons from Src-Family Tyrosine Kinases. *Acc Chem Res.* 2017; 50:1193–1201. [PubMed: 28426203]
41. Chang CA, Roberts CC, Tang Z. Understanding Ligand-Receptor Non-Covalent Binding Kinetics Using Molecular Modeling. *Front Biosci Landmark Ed.* 2017; 22:960–981. [PubMed: 27814657]
42. Yang LJ, Zou J, Xie HZ, Li LL, Wei YQ, Yang SY. Steered Molecular Dynamics Simulations Reveal the Likelier Dissociation Pathway of Imatinib from its Targeting Kinases C-Kit and Abl. *PLoS One.* 2009; 4:e8470. [PubMed: 20041122]
43. Capelli AM, Costantino G. Unbinding Pathways of VEGFR2 Inhibitors Revealed by Steered Molecular Dynamics. *J Chem Inf Model.* 2014; 54:3124–3136. [PubMed: 25299731]
44. Patel JS, Berteotti A, Ronsisvalle S, Rocchia W, Cavalli A. Steered Molecular Dynamics Simulations for Studying Protein–Ligand Interaction in Cyclin-Dependent Kinase 5. *J Chem Inf Model.* 2014; 54:470–480. [PubMed: 24437446]
45. Callegari D, Lodola A, Pala D, Rivara S, Mor M, Rizzi A, Capelli AM. Metadynamics Simulations Distinguish Short- and Long-Residence-Time Inhibitors of Cyclin-Dependent Kinase 8. *J Chem Inf Model.* 2017; 57:159–169. [PubMed: 28080056]
46. Kong X, Sun H, Pan P, Tian S, Li D, Li Y, Hou T. Molecular Principle of the Cyclin-Dependent Kinase Selectivity of 4-(thiazol-5-yl)-2-(phenylamino) pyrimidine-5-carbonitrile Derivatives Revealed by Molecular Modeling Studies. *Phys Chem Chem Phys.* 2016; 18:2034–2046. [PubMed: 26686753]
47. Kong X, Sun H, Pan P, Zhu F, Chang S, Xu L, Li Y, Hou T. Importance of Protein Flexibility on Molecular Recognition: A Case Study on Type-II/2 Inhibitors of ALK. *Phys Chem Chem Phys.* 2018; 20:4851–4863. [PubMed: 29383359]
48. Niu Y, Li S, Pan D, Liu H, Yao X. Computational Study on the Unbinding Pathways of B-RAF Inhibitors and its Implication for the Difference of Residence Time: Insight from Random Acceleration and Steered Molecular Dynamics Simulations. *Phys Chem Chem Phys.* 2016; 18:5622–5629. [PubMed: 26862741]
49. Niu Y, Pan D, Yang Y, Liu H, Yao X. Revealing the Molecular Mechanism of Different Residence Times of ERK2 Inhibitors via Binding Free Energy Calculation and Unbinding Pathway Analysis. *Chemom Intell Lab Syst.* 2016; 158:91–101.
50. Wang Z, Canagarajah BJ, Boehm JC, Kassisa S, Cobb MH, Young PR, Abdel-Meguid S, Adams JL, Goldsmith EJ. Structural Basis of Inhibitor Selectivity in MAP Kinases. *Structure (Oxford, U. K.).* 1998; 6:1117–1128.
51. Simard JR, Getlik M, Grutter C, Pawar V, Wulfert S, Rabiller M, Rauh D. Development of a Fluorescent-Tagged Kinase Assay System for the Detection and Characterization of Allosteric Kinase Inhibitors. *J Am Chem Soc.* 2009; 131:13286–13296. [PubMed: 19572644]
52. Gill AL, Frederickson M, Cleasby A, Woodhead SJ, Carr MG, Woodhead AJ, Walker MT, Congreve MS, Devine LA, Tisi D, O'Reilly M, Seavers LC, Davis DJ, Curry J, Anthony R, Padova

- A, Murray CW, Carr RA, Jhoti H. Identification of Novel P38alpha MAP Kinase Inhibitors Using Fragment-Based Lead Generation. *J Med Chem.* 2005; 48:414–426. [PubMed: 15658855]
53. Pargellis C, Tong L, Churchill L, Cirillo PF, Gilmore T, Graham AG, Grob PM, Hickey ER, Moss N, Pav S, Regan J. Inhibition of P38 MAP Kinase by Utilizing a Novel Allosteric Binding Site. *Nat Struct Biol.* 2002; 9:268–272. [PubMed: 11896401]
54. Case, DA., et al. AMBER. Vol. 14. University of California; San Francisco: 2014.
55. Case DA, Cheatham TE3rd, Darden T, Gohlke H, Luo R, Merz KM Jr, Onufriev A, Simmerling C, Wang B, Woods RJ. The Amber Biomolecular Simulation Programs. *J Comput Chem.* 2005; 26:1668–1688. [PubMed: 16200636]
56. Hornak V, Abel R, Okur A, Strockbine B, Roitberg A, Simmerling C. Comparison of Multiple Amber Force Fields and Development of Improved Protein Backbone Parameters. *Proteins: Struct, Funct Genet.* 2006; 65:712–725. [PubMed: 16981200]
57. Okur A, Strockbine B, Hornak V, Simmerling C. Using PC Clusters to Evaluate the Transferability of Molecular Mechanics Force Fields for Proteins. *J Comput Chem.* 2003; 24:21–31. [PubMed: 12483672]
58. Phillips JC, Braun R, Wang W, Gumbart J, Tajkhorshid E, Villa E, Chipot C, Skeel RD, Kale L, Schulten K. Scalable Molecular Dynamics with NAMD. *J Comput Chem.* 2005; 26:1781–1802. [PubMed: 16222654]
59. Graf J, Nguyen PH, Stock G, Schwalbe H. Structure and Dynamics of the Homologous Series of Alanine Peptides: A Joint Molecular Dynamics/NMR Study. *J Am Chem Soc.* 2007; 129:1179–1189. [PubMed: 17263399]
60. Wickstrom L, Okur A, Simmerling C. Evaluating the Performance of the ff99SB Force Field Based on NMR Scalar Coupling Data. *Biophys J.* 2009; 97:853–856. [PubMed: 19651043]
61. Gilson MK, Gilson HSR, Potter MJ. Fast Assignment of Accurate Partial Atomic Charges: An Electronegativity Equalization Method that Accounts for Alternate Resonance Forms. *J Chem Inf Model.* 2003; 43:1982–1997.
62. Essmann U, Perera L, Berkowitz ML, Darden T, Lee H, Pedersen LG. A Smooth Particle Mesh Ewald Method. *J Chem Phys.* 1995; 103:8577–8593.
63. Ryckaert J-P, Ciccotti G, Berendsen HJC. Numerical Integration of the Cartesian Equations of Motion of a System with Constraints: Molecular Dynamics of N-Alkanes. *J Comput Phys.* 1977; 23:327–341.
64. Hamelberg D, Mongan J, McCammon JA. Accelerated Molecular Dynamics: A Promising and Efficient Simulation Method for Biomolecules. *J Chem Phys.* 2004; 120:11919–11929. [PubMed: 15268227]
65. Tang Z, Chang C-eA. Systematic Dissociation Pathway Searches Guided by Principal Component Modes. *J Chem Theory Comput.* 2017; 13:2230–2244. [PubMed: 28418661]
66. Kumar S, Rosenberg JM, Bouzida D, Swendsen RH, Kollman PA. THE Weighted Histogram Analysis Method for Free-Energy Calculations on Biomolecules. *J Comput Chem.* 1992; 13:1011–1021.
67. Souaille M, Roux Bt. Extension to the Weighted Histogram Analysis Method: Combining Umbrella Sampling with Free Energy Calculations. *Comput Phys Commun.* 2001; 135:40–57.
68. Ai R, Qaiser Fatmi M, Chang CE. T-Analyst: A Program for Efficient Analysis of Protein Conformational Changes by Torsion Angles. *J Comput-Aided Mol Des.* 2010; 24:819–827. [PubMed: 20689979]
69. Mondal J, Friesner RA, Berne BJ. Role of Desolvation in Thermodynamics and Kinetics of Ligand Binding to a Kinase. *J Chem Theory Comput.* 2014; 10:5696–5705. [PubMed: 25516727]
70. Pearlstein RA, Sherman W, Abel R. Contributions of Water Transfer Energy to Protein-Ligand Association and Dissociation Barriers: Watermap Analysis of a Series of P38alpha MAP Kinase Inhibitors. *Proteins: Struct, Funct Genet.* 2013; 81:1509–1526. [PubMed: 23468227]
71. Mueller-Fahrnow A, Andres D, Fernandez-Montalvan AE, Stegmann CM, Becker A, Georgi V. Binding Kinetics in Drug Discovery - A Current Perspective. *Front Biosci Landmark Ed.* 2017; 22:21–47. [PubMed: 27814600]
72. Tiwary P, Berne BJ. How Wet Should Be the Reaction Coordinate for Ligand Unbinding? *J Chem Phys.* 2016; 145:054113. [PubMed: 27497545]

73. Setny P, Baron R, Michael Kekenes-Huskey P, McCammon JA, Dzubiella J. Solvent Fluctuations in Hydrophobic Cavity–Ligand Binding Kinetics. *Proc Natl Acad Sci U S A*. 2013; 110:1197–1202. [PubMed: 23297241]
74. Huang, Y-mM, Raymundo, MAV., Chen, W., Chang, C-eA. Mechanism of the Association Pathways for a Pair of Fast and Slow Binding Ligands of HIV-1 Protease. *Biochemistry*. 2017; 56:1311–1323. [PubMed: 28060481]
75. Mittal J, Hummer G. Static and Dynamic Correlations in Water at Hydrophobic Interfaces. *Proc Natl Acad Sci U S A*. 2008; 105:20130–20135. [PubMed: 19074279]
76. Tiwary P, Mondal J, Morrone JA, Berne BJ. Role of Water and Steric Constraints in the Kinetics of Cavity–Ligand Unbinding. *Proc Natl Acad Sci U S A*. 2015; 112:12015–12019. [PubMed: 26371312]
77. Weiß RG, Setny P, Dzubiella J. Principles for Tuning Hydrophobic Ligand–Receptor Binding Kinetics. *J Chem Theory Comput*. 2017; 13:3012–3019. [PubMed: 28494155]
78. Izadi S, Onufriev AV. Accuracy Limit of Rigid 3-Point Water Models. *J Chem Phys*. 2016; 145:074501. [PubMed: 27544113]
79. Agafonov RV, Wilson C, Otten R, Buosi V, Kern D. Energetic Dissection of Gleevec’s Selectivity toward Human Tyrosine Kinases. *Nat Struct Mol Biol*. 2014; 21:848–853. [PubMed: 25218445]
80. Diskin R, Askari N, Capone R, Engelberg D, Livnah O. Active Mutants of the Human P38alpha Mitogen-Activated Protein Kinase. *J Biol Chem*. 2004; 279:47040–47049. [PubMed: 15284239]
81. Casper D, Bukhtiyarova M, Springman EB. A Biacore Biosensor Method for Detailed Kinetic Binding Analysis of Small Molecule Inhibitors of P38alpha Mitogen-Activated Protein Kinase. *Anal Biochem*. 2004; 325:126–136. [PubMed: 14715293]
82. Regan J, Pargellis CA, Cirillo PF, Gilmore T, Hickey ER, Peet GW, Proto A, Swinamer A, Moss N. The Kinetics of Binding to P38MAP Kinase by Analogues of BIRB 796. *Bioorg Med Chem Lett*. 2003; 13:3101–3104. [PubMed: 12941343]

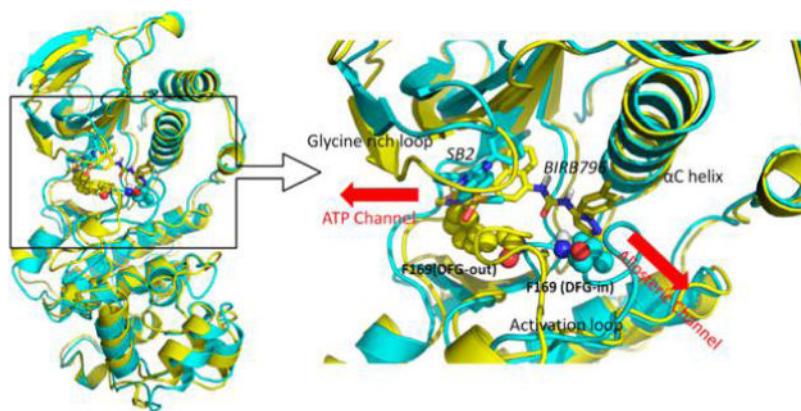


Figure 1. Comparison of crystal structures of p38 α in DFG-in and DFG-out conformations. The left figure shows the structure alignment of DFG-in (cyan, PDB 1A9U) and DFG-out (yellow, PDB 1KV2) conformations bound with ligands SB2 and BIRB796, respectively. The right figure shows binding site structures. The Phe169 from the DFG motif is shown in sphere structure; ligands SB2 and BIRB796 are shown in licorice structure.

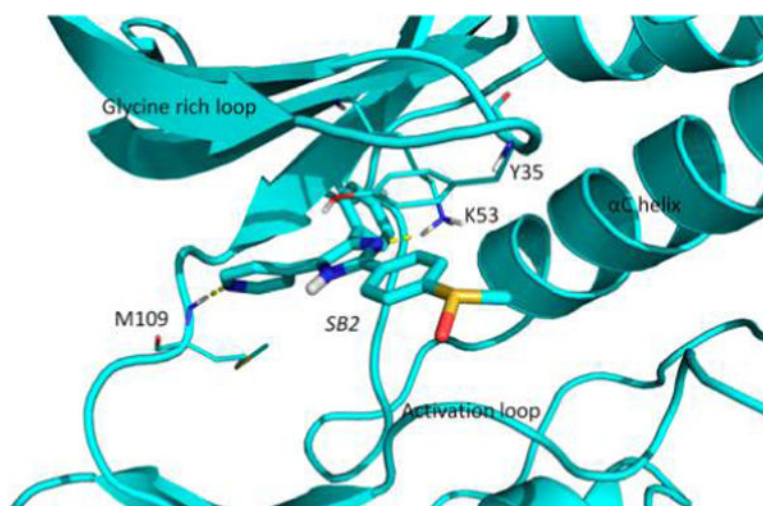


Figure 2. Interactions between SB2 and p38 α in DFG-in conformation from crystal structure (PDB ID: 1A9U). SB2 is shown in bold licorice structure. Key interacting residues are shown in thin licorice structure. Hydrogen bonds between SB2 and p38 α are shown as dashed lines.

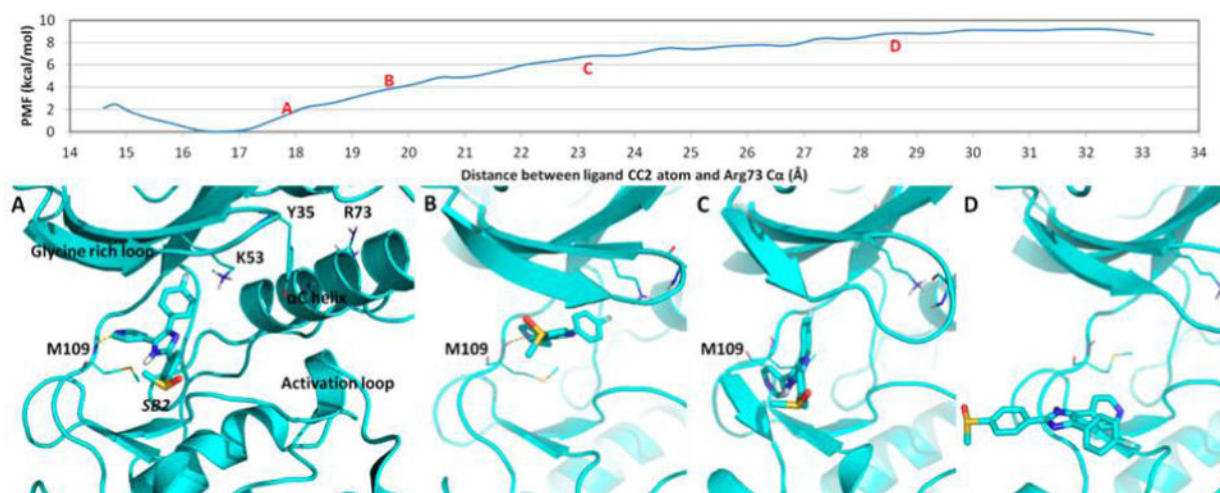


Figure 3. PMF of dissociation process of SB2 (DFG-in) and selected snapshots from umbrella sampling. SB2 is shown in bold licorice structure. Key interacting residues are shown in thin licorice structure. Hydrogen bonds between SB2 and p38 α are shown as dashed lines.

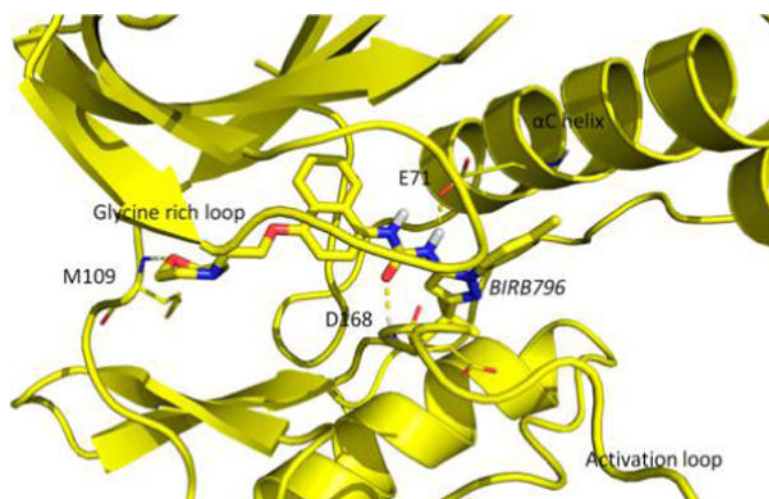


Figure 4. Interactions between BIRB796 and p38 α in DFG-out conformation from crystal structure (PDB ID: 1KV2). BIRB796 is shown in bold licorice structure. Key interacting residues are shown in thin licorice structure. Hydrogen bonds between BIRB796 and p38 α are shown as dashed lines.

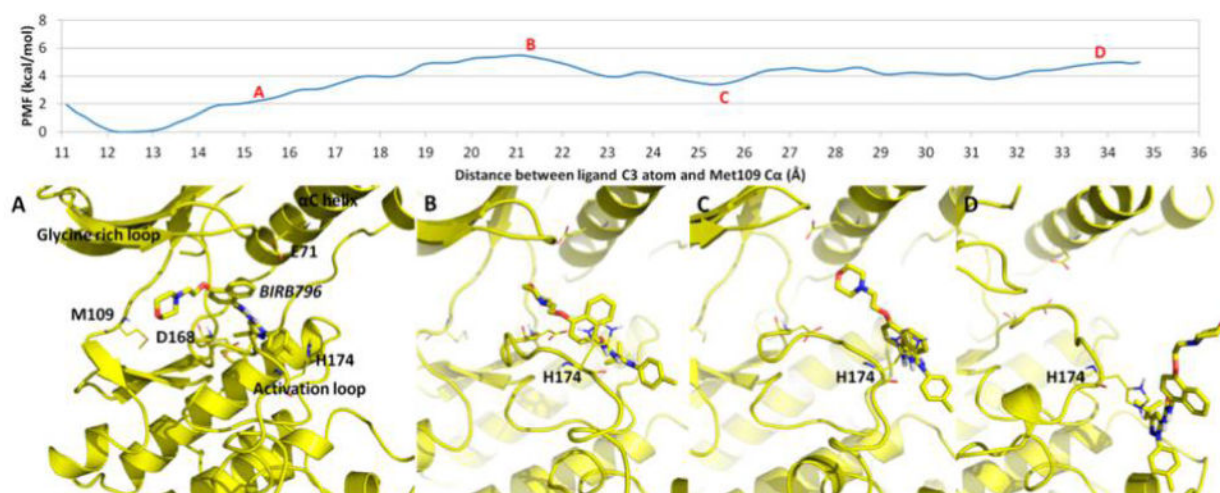


Figure 5. PMF of dissociation process of BIRB796 along allosteric pathway and selected snapshots from umbrella sampling. BIRB796 is shown in bold licorice structure. Key interacting residues are shown in thin licorice structure.

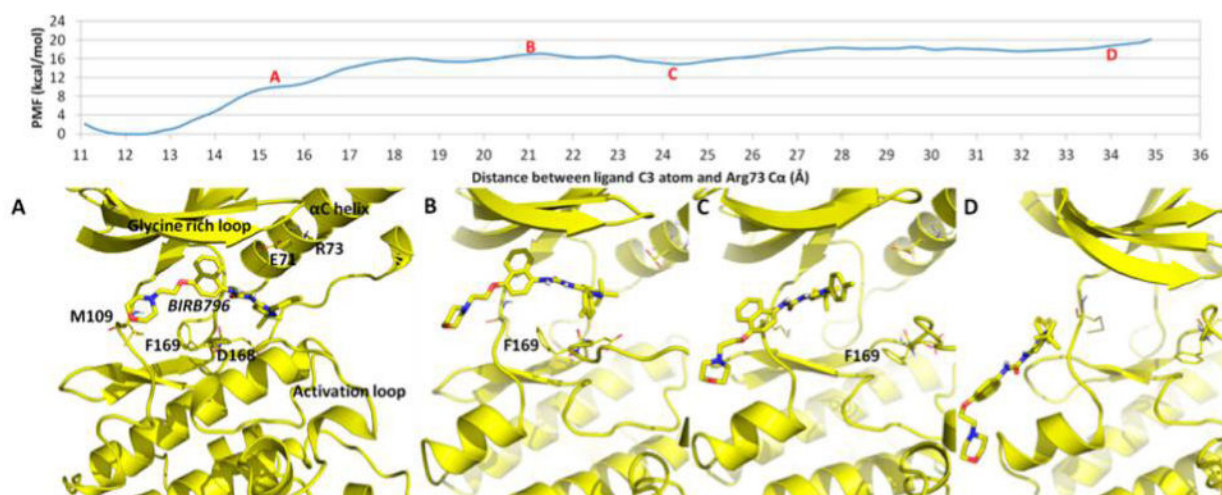


Figure 6. PMF of dissociation process of BIRB796 along ATP pathway and selected snapshots from umbrella sampling. BIRB796 is shown in bold licorice structure. Key interacting residues are shown in thin licorice structure.

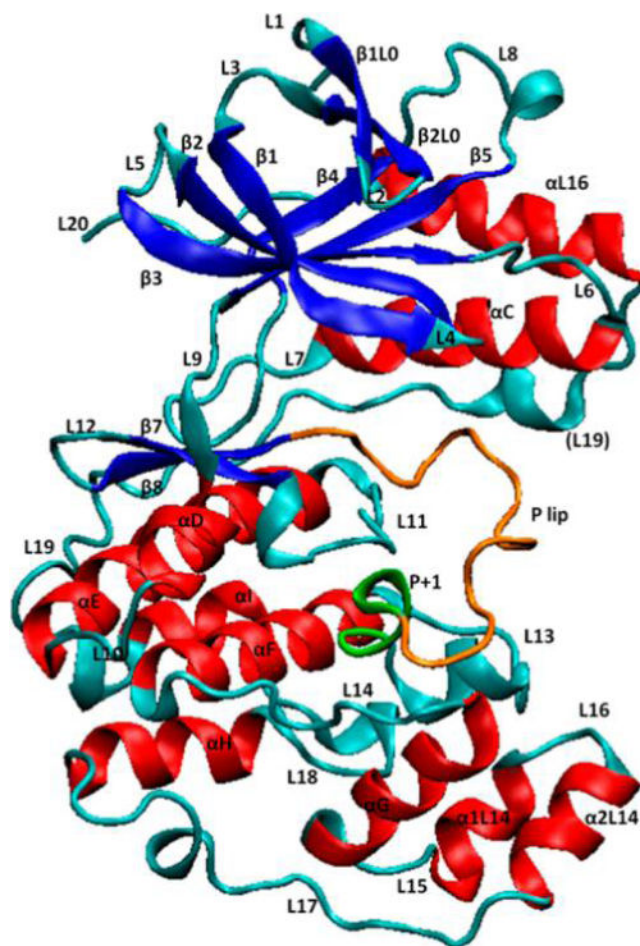


Figure 7. Division of p38 α protein into different fragments basing on the secondary structure of protein. The α -helix is colored red, the β -sheet is colored blue, the loop is colored cyan, the activation loop is colored orange, and the P+1 substrate site is colored green.

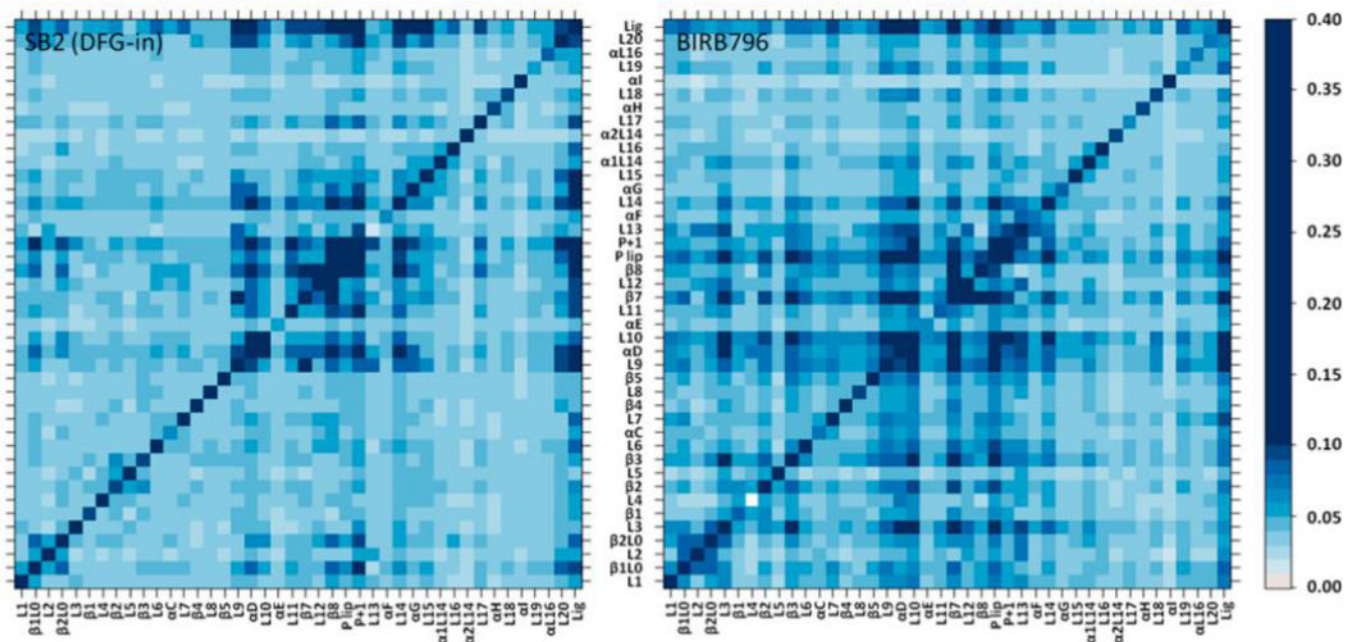


Figure 8. Correlation maps of SB2 (bound to DFG-in conformation) and BIRB796 p38 α complexes during the dissociation process.

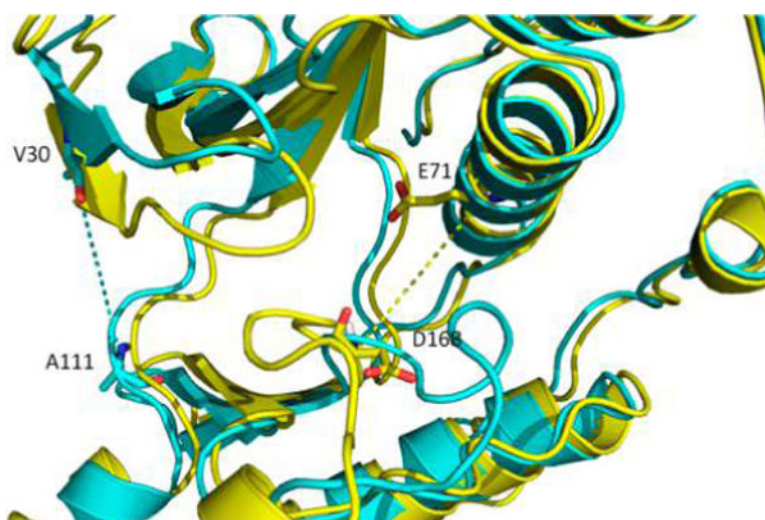


Figure 9. Distance used as RC for hinge motions. Hinge distances are indicated by the distance between $C\alpha$ of Glu71 and Asp168, which is on the allosteric path of type-II/III ligands (yellow), and the distance between $C\alpha$ of Val30 and Ala111, which is on the ATP path of type-I ligand (cyan).

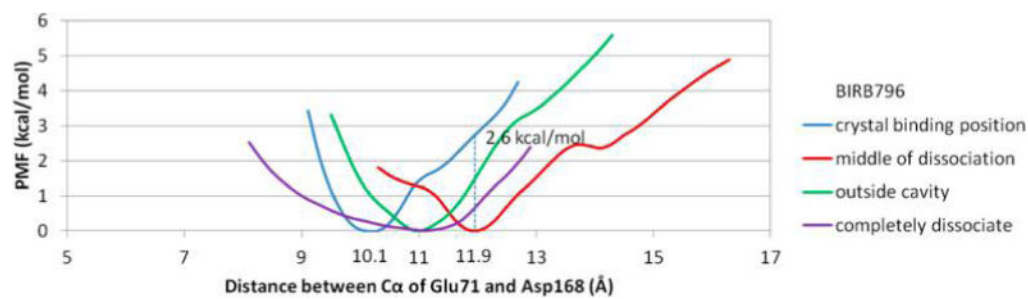


Figure 10.

Free energy change along hinge movement of p38 α in DFG-out conformation at different stages of dissociation of BIRB796. The distance between C α of Glu71 and Asp168 is used as the RC.

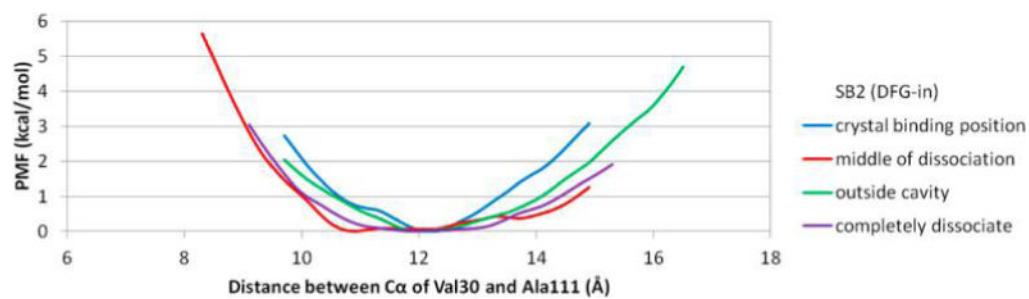


Figure 11. Free energy change along hinge movement of p38 α in DFG-in conformation at different stages of dissociation of SB2. The distance between C α of Val30 and Ala111 is used as the RC.

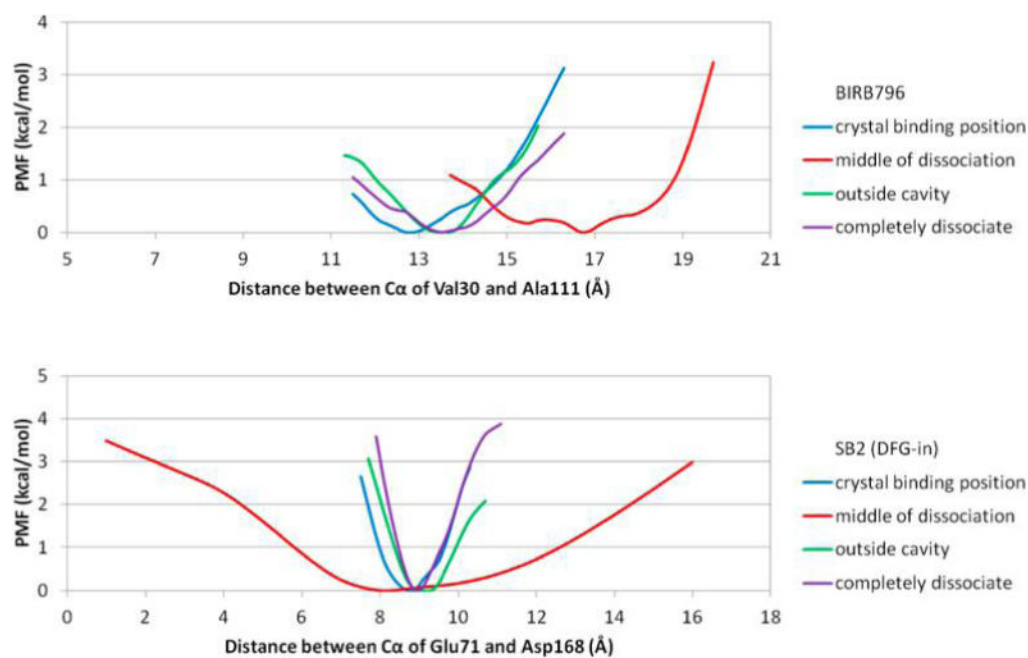


Figure 12. Free energy change along hinge movement of p38 α at different stages of dissociation of BIRB796 and SB2 (DFG-in). The distance between C α of Val30 and Ala111 is used as the RC for BIRB796. The distance between C α of Glu71 and Asp168 is used as the RC for SB2 (DFG-in).

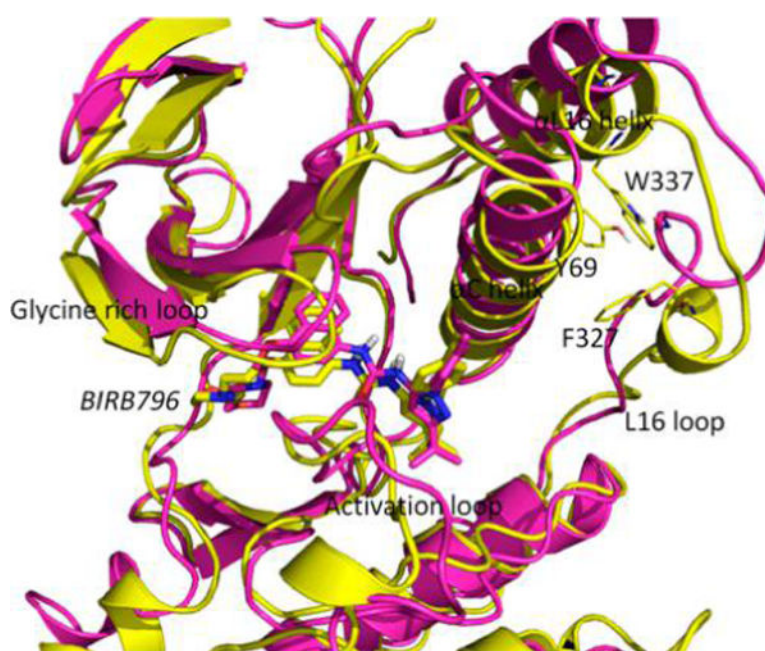


Figure 13. Superposition of representative structures of wild p38 α - BIRB796 complex (yellow) and its mutated structure (pink) from CMD simulations. Residues Tyr69, Phe327, and Trp337 are mutated to glycine. Ligand BIRB796 is shown in bold licorice structure. Tyr69, Phe327, Trp337, and their mutated glycine form are shown in thin licorice structure.

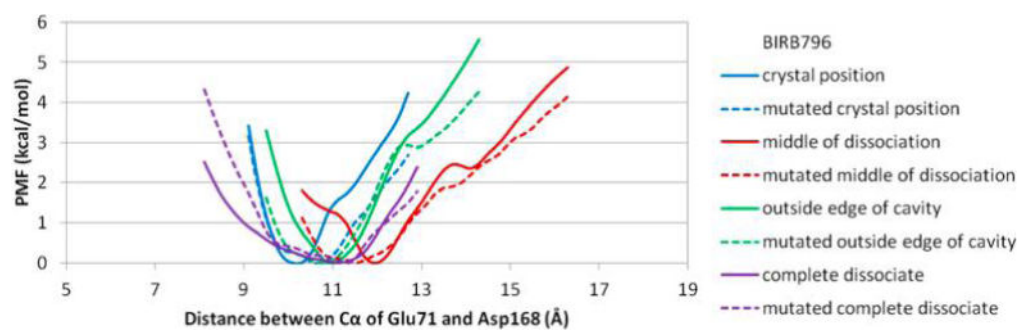
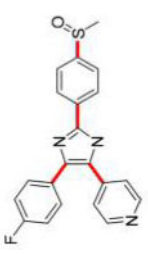
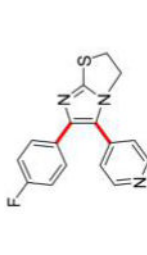
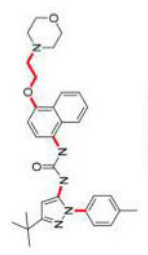
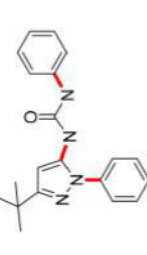


Figure 14. Free energy change along hinge movement of p38 α in DFG-out conformation at different stages of dissociation of BIRB796 before and after mutation. The distance between C α of Glu71 and Asp168 is used as the RC.

Table 1
Chemical Structures, Interaction Modes, and Protein Kinase Activity of p38 α Inhibitors Used in the Study^a

No	Structure	K _D (nM)	k _{onl} [M ⁻¹ s ⁻¹]	k _{off} [s ⁻¹]	G _{exp} (kcal/mol)	PDB ID	Mode
1	 SB2	11.5	1.5×10 ⁷	1.8×10 ⁻¹	-10.9	1A9U (3GCP)	DFG-in (DFG-out)
2	 SK8	180	4.3×10 ⁷	7.7	-9.7	N/A	DFG-in
3	 BIRB796	0.1	8.4×10 ⁴	8.3×10 ⁻⁶	-13.7	1KV2	DFG-out
4	 LIG4	21	7.3×10 ⁴	1.6×10 ⁻³	-10.5	N/A	DFG-out

^a Rotatable dihedral angles of p38 α inhibitors are highlighted in red. K_D, k_{on}, and k_{off} were taken from refs^{53, 81, and 82}.